Evaluation of PNT Situational Awareness Algorithms and Methods

Sandeep Jada, Mark Psiaki, Sean Landerkin, *Virginia Tech*
Steven Langel, Arthur Scholz, *The MITRE Corporation*
Mathieu Joerger, *Virginia Tech*

BIOGRAPHY

Sandeep Jada obtained a masters degree (2011) in aerospace engineering from Indian Institute of Science, Bangalore, India. He worked for Airbus India (2011 to 2018). He is a doctoral candidate at Virginia Tech working with Dr Mathieu Joerger, with a focus on error time correlation modeling and GNSS interference detection.

Mark Psiaki is Professor and Kevin T. Crofton Faculty Chair of Aerospace and Ocean Engineering at Virginia Tech. He is also Professor Emeritus of Mechanical and Aerospace Engineering at Cornell University. He holds a Ph.D. in Mechanical and Aerospace Engineering from Princeton University. He is a Fellow of both the ION and the AIAA. His research interests are in the areas of navigation, spacecraft attitude and orbit determination, remote sensing, and general methods for estimation, filtering, and detection.

Sean Landerkin obtained a bachelor's degree in aerospace engineering from Virginia Tech in 2021. He is currently working for Raytheon Technologies as a systems engineer on NOAA's Joint Polar Satellite System (JPSS).

Steven Langel received his Ph.D. in mechanical and aerospace engineering from the Illinois Institute of Technology (IIT), Chicago, IL, USA. He is currently a lead signal processing engineer at The MITRE Corporation, Bedford, MA, USA, focusing on the development of multi-sensor navigation and fault detection algorithms. He is also pursuing research in robust estimation algorithms for safety-critical applications. Steve has been a member of the MITRE technical staff since 2014.

Arthur Scholz is a Principal Engineer and leads the NAVWAR and Robust PNT Group at the MITRE Corporation where he has worked on PNT projects across the defense and civilian sectors. Prior to joining MITRE in 2015, Arthur worked as a research scientist in the chemical industry. He received his Ph.D in Materials Science from the University of California, Santa Barbara.

Mathieu Joerger (M.S., INSA Strasbourg - Illinois Tech, 2002; Ph.D., Illinois Tech 2009) is assistant professor at Virginia Tech, senior editor of Navigation for IEEE TAES, member of EU/US Cooperation on Satellite Navigation, Working Group C - ARAIM.

ABSTRACT

This paper describes the design and evaluation of new GNSS jamming detection methods for position, navigation and timing (PNT) situational awareness (SA). These methods are intended for implementation over large networks of GNSS receivers. We focus on jamming threats caused by personal privacy devices (PPDs). We first derive two new jamming detection tests to identify events of simultaneous drops in C/N0 impacting all satellites in view. To limit the risk of false alerts, we develop an automated process to model satellite-specific and receiver-station-specific C/N0 measurement variations under jamming-free conditions. These models are then incorporated in our new detectors and evaluated using months of GPS L1 C/N0 data from continuously operating reference stations (CORS). Tens to hundreds of events are detected monthly at CORS sites located next to highways. To confirm that the detected events are caused by jamming, we analyze CORS data over multiple days at multiple locations, and find patterns in jamming schedules. In addition, we process ADS-B-reported aircraft receiver data during two known radio-frequency interference (RFI) events that also impacted CORS data.

I. INTRODUCTION

In this paper, we describe the design and preliminary evaluation of algorithms and methods for positioning, navigation and timing (PNT) situational awareness. We focus on detection of jamming events, including those caused by Personal Privacy Devices (PPDs) [1], because the probability of occurrence of such events is high, which increases opportunities for observations "in the wild" of illegal Radio Frequency Interference (RFI) in GNSS bands. This paper shows that tens of events can be observed monthly at locations next to major highways using data that is publicly available.

 https://doi.org/10.33012/2021.17935

The threat of RFI on GNSS-based PNT, including jamming and spoofing, has been growing over the past decade [2]. Multiple localized research efforts have provided innovative means to detect such threats [3]. The methods proposed in [4–7] use sophisticated signal processing techniques and dedicated hardware. However, such approaches may be too expensive for widespread deployment, and therefore do not address the need for a wide-scale RFI detection system. Automatic Gain Control (AGC) was used as a measure of signal power to detect jamming incidents at an example location over multiple weeks in [8]. Unfortunately, AGC is not readily provided by existing networks of GNSS receivers. Other attempts at detecting RFI are based on aircraft Automatic Dependent Surveillance – Broadcast (ADS-B), for example using absence of responses or the Navigational Integrity Category (NIC) [9, 10]. Non-RFI factors, however, impact these parameters, which cause false detections, and publicly-available ADS-B databases rely on unknown third-party sources that are prone to recording, storing, and formatting errors [11]. Promising results for jamming detection using crowd-sourced Carrier-to-Noise ratio (C/N0) parameters are found in [12–16]. An effective C/N0-based jamming detector was also proposed in [17].

In this paper, we evaluate the potential of receiver network C/N0-based and ADS-B parameter-based monitoring methods to detect jamming incidents over wide areas, and over periods of several months.

A major challenge in C/N0-based monitoring over wide areas is in detection threshold setting at different network receivers. We want to set thresholds to limit the risk of false alert, i.e., the probability of detection under nominal, no-jamming conditions. Nominal C/N0 conditions vary widely from one location to another depending on the receiver's multipath environment. In addition, receivers and antennas at different locations may not be of the same model and brand, as is the case in the National Geodetic Survey's (NGS) Continuously Operating Reference Stations (CORS) network. We must develop a systematic method, which can be automated for use at hundreds of locations, to determine a receiver's nominal C/N0 variations. This method must account for the facts that nominal C/N0 values differ across satellites, and that the impact of multipath varies as the line-of-sight from static reference-station antenna to satellite changes over time.

We implement the resulting jamming-free C/N0 models in detection tests aimed at minimizing the probability of no detection while achieving a predefined risk of false alert. Rather than using chi-squared C/N0-residuals to monitor any type of C/N0 variation, we derive two new, more sensitive test statistics specifically designed to detect simultaneous C/N0-drops on all satellites in view caused by jamming. We evaluate these detection methods using publicly-available CORS GPS L1 C/N0 data.

In order to gain confidence that the detected events are jamming events, which we suspect are caused by personal privacy devices (PPD) on road vehicles, we process data from multiple CORS sites along a highway. In addition, we analyze CORS and ADS-B data during known RFI events caused by military testing.

The organization of this paper is as follows. In Sec. II we derive two optimal hypothesis tests, one using C/N0 and another using time-differenced C/N0. Then, in Sec. III, we develop probabilistic models of nominal C/N0 variations as a function of space vehicle (SV) azimuth and elevation angles to a ground reference receiver antenna. Sec. IV shows the CORS data analysis using the two new jamming detection methods at an example location over May to July 2021. Sec. V describes the multi-location CORS and ADS-B data analyses to consolidate the detection of actual jamming events. Sec. VI presents our conclusions.

II. C/N0-BASED JAMMING DETECTION TEST DERIVATION

In this section, we derive two new methods to detect the presence of jamming using C/N0 measurements of all SVs in view.

1. C/N0-Residual Projection Test for Jamming Detection

Let '$C_{i,k}$' be the received power in watts from SV i, at time-step k, and let '$N0$' be the thermal noise power density in watts/Hz (W/Hz). On a log scale, C/N0 can be expressed in decibel-Hz (dB-Hz) as:

$$\left(\frac{C_{i,k}}{N_0}\right)_{dB-Hz} \triangleq 10\ log_{10}\left(\frac{C_{i,k}}{N_0}\right) \tag{1}$$

We assume that C/N0 in dB-Hz is normally distributed with mean $\mu_{i,k}$ and variance $\sigma^2_{i,k}$. We use the notation:

$$\left(\frac{C_{i,k}}{N_0}\right)_{dB-Hz} \sim N(\mu_{i,k}, \sigma^2_{i,k}). \tag{2}$$

We will evaluate and refine this assumption in Sec. III. In the presence of a jammer broadcasting in the bandwidth of the radio-frequency (RF) front end, the jamming power density J_k is added to $N0$ in the denominator of Eq.1. J_k (in W/Hz) is the average jamming power density at time-step k: it is the received jamming power divided by the bandwidth of RF front-end. We can write the carrier-to-noise-plus-jamming ratio as,

$$\left(\frac{C_{i,k}}{N_0 + J_k}\right)_{dB-Hz} = 10\ log_{10}\left(\frac{C_{i,k}}{N_0 + J_k}\right) = \left(\frac{C_{i,k}}{N_0}\right)_{dB-Hz} - \gamma_k \tag{3}$$

where the jamming power density parameter is defined as:

$$\gamma_k \triangleq 10\ log_{10}\left(1 + \frac{J_k}{N_0}\right) \tag{4}$$

Parameter γ_k varies with J_k. Thus, in the presence of a jammer, a receiver's measured C/N0 distribution can be expressed as:

$$c_{i,k} \triangleq \left(\frac{C_{i,k}}{N_0 + J_k}\right)_{dB-Hz} \sim N(\mu_{i,k} - \gamma_k, \sigma_{i,k}^2) \tag{5}$$

The unknown quantity γ_k in Eq.5 is an indicator of the jamming events we want to detect.

We want to derive a test to detect jamming using C/N0 measurements from all SVs in view at time k. We first define the observation vector, when jamming is present ($J_k \neq 0$) or not ($J_k = 0$), as:

$$\boldsymbol{c}_k = [c_{1,k}, \ldots, c_{n,k}]^T \tag{6}$$

where n is the number of SVs in view at time k. Boldface fonts are used for vectors and matrices. C/N0 measurements are assumed to be uncorrelated across satellites.

We distinguish two mutually-exclusive, exhaustive hypotheses of no jamming, H_0, and jamming, H_1, which are defined as:

$$\begin{aligned} \text{null hypothesis } H_0 : \gamma_k = 0 \implies J_k = 0 \text{ (no jamming)} \\ \text{alternate hypothesis } H_1 : \gamma_k > 0 \implies J_k > 0 \text{ (jamming)} \end{aligned} \tag{7}$$

The probability density functions (PDF) of measured C/N0 under the two hypotheses can be written as:

$$\begin{aligned} p\left(\boldsymbol{c}_k \middle| H_0\right) &= \frac{1}{\sqrt{(2\pi)^n |\boldsymbol{S}_k|}}\ exp\left(-\frac{1}{2}(\boldsymbol{c}_k - \boldsymbol{\mu}_k)^T \boldsymbol{S}_k^{-1} (\boldsymbol{c}_k - \boldsymbol{\mu}_k)\right) \\ p\left(\boldsymbol{c}_k \middle| H_1\right) &= \frac{1}{\sqrt{(2\pi)^n |\boldsymbol{S}_k|}}\ exp\left(-\frac{1}{2}(\boldsymbol{c}_k - \boldsymbol{\mu}_k + \mathbf{1}\gamma_k)^T \boldsymbol{S}_k^{-1} (\boldsymbol{c}_k - \boldsymbol{\mu}_k + \mathbf{1}\gamma_k)\right) \end{aligned} \tag{8}$$

where, $|\boldsymbol{S}_k|$ is the determinant of the positive definite matrix $\boldsymbol{S}_k$, $\boldsymbol{\mu}_k = [\mu_{1,k}, \ldots, \mu_{n,k}]^T$ is the vector of mean C/N0s for all SVs in view, $\mathbf{1} = [1, \ldots, 1]^T$ is an $n \times 1$ vector of ones, and $\boldsymbol{S}_k = diag\left(\left[\sigma_{1,k}^2, \ldots, \sigma_{n,k}^2\right]\right)$ is the covariance matrix of the observation vector. We use the Neyman-Pearson lemma to express the test statistic that minimizes the probability of missed detection (P_{MD}) as:

$$\Lambda_k(\boldsymbol{c}_k, \gamma_k) = ln\left(\frac{P\left(\boldsymbol{c}_k \middle| H_1\right)}{P\left(\boldsymbol{c}_k \middle| H_0\right)}\right) \tag{9}$$

where, $ln()$ is the natural logarithm function. Substituting Eq. 8 into Eq. 9, we obtain the following test statistic equation:

$$\Lambda_k(\boldsymbol{c}_k, \gamma_k) = -(\boldsymbol{c}_k - \boldsymbol{\mu}_k)^T \boldsymbol{S}_k^{-1} \mathbf{1}\gamma_k - \frac{1}{2}\mathbf{1}^T \boldsymbol{S}_k^{-1} \mathbf{1}\gamma_k^2 \tag{10}$$

Since the jamming power and jammer locations are unknown, parameter γ_k is unknown. We can derive the locally most powerful test statistic for small jamming power ($\gamma_k \to 0$) as:

$$\alpha_k \triangleq \left.\frac{\partial \Lambda_k(\boldsymbol{c}_k, \gamma_k)}{\partial \gamma_k}\right|_{\gamma_k = 0} = -(\boldsymbol{c}_k - \boldsymbol{\mu}_k)^T \boldsymbol{S}_k^{-1} \mathbf{1} \tag{11}$$

Under H_0, the test statistic α_k is distributed as:

$$\alpha_k \sim N\left(0, \mathbf{1}^T \boldsymbol{S}_k^{-1} \mathbf{1}\right) \tag{12}$$

The detection threshold T_k is set to meet a predefined requirement on the probability of false alert $P_{FA,REQ}$. T_k is derived from the following equation:

$$P_{FA,REQ} = P(\alpha_k > T_k | H_0) \tag{13}$$

The detection test is locally optimal at $\gamma_k = 0$, i.e., for detecting simultaneous drops in C/N0 even if these are small in magnitude. The test is one-sided, i.e., it aims at detecting drops in C/N0 without triggering an alert in the case of C/N0-increases. It is worth noting that this test can not only be used at one instant but also over fixed time-intervals. In the latter case, observation vectors $\boldsymbol{c}_k$ can be stacked over a time-window, and the test can be implemented using a sliding window mechanism. This method would efficiently detect lasting jamming events. It is not implemented in this paper because the events we seek are of short duration, caused by PPDs on road vehicles passing by static CORS receivers.

The computation of α_k in Eq.11 using the observation vector $\boldsymbol{c}_k$ requires an estimate of the mean jamming-free C/N0 vector $\boldsymbol{\mu}_k = [\mu_{1,k} \ldots \mu_{n,k}]^T$ and covariance matrix $\boldsymbol{S}_k = diag\left(\left[\sigma^2_{1,k} \ldots \sigma^2_{n,k}\right]\right)$. We describe our approach for modeling the mean and variance of C/N0 using experimental data in SectionIII.

2. Time-Differenced C/N0 Test for Jamming Detection

In contrast to the method described above, jamming detection using time-differenced C/N0 only requires a variance model because time-differencing C/N0 over short time-intervals eliminates the mean C/N0 value. This test is useful, especially when first processing a set of data for which the mean C/N0 model is unknown. A time-differenced C/N0 measurement $\Delta c_{i,k}$ under jamming is defined as:

$$\Delta c_{i,k} \triangleq 10\ log_{10}\left(\frac{C_{i,k}}{N_0 + J_k}\right) - 10\ log_{10}\left(\frac{C_{i,k-1}}{N_0 + J_{k-1}}\right) \tag{14}$$

Rearranging terms and substituting Eq. 3 into the resulting equation gives the following expression:

$$\Delta c_{i,k} = \left(\frac{C_{i,k}}{N_0}\right)_{dB-Hz} - \left(\frac{C_{i,k-1}}{N_0}\right)_{dB-Hz} - \Delta\gamma_k \tag{15}$$

where $\Delta\gamma_k$ is defined as: $\Delta\gamma_k \triangleq (\gamma_k - \gamma_{k-1})$. Jamming power variations impact $\Delta\gamma_k$. The distribution of $\Delta c_{i,k}$ can be expressed as:

$$\Delta c_{i,k} \sim N(-\Delta\gamma_k, \sigma^2_{\Delta i,k}) \tag{16}$$

where the variance $\sigma^2_{\Delta i,k}$ will be evaluated in Sec. III and the mean of $\Delta c_{i,k}$ is $-\Delta\gamma_k$ because $(\mu_{i,k} - \mu_{i,k-1} \sim 0)$ over short time intervals, e.g., over $k - (k-1) = 1$s.

We want to derive a test to detect jamming signal from time-differenced C/N0s for all n SVs in view at time-step k. We define the observation vector as:

$$\boldsymbol{\Delta c}_k \triangleq \boldsymbol{c}_k - \boldsymbol{c}_{k-1} = [\Delta c_{1,k} \ldots \Delta c_{n,k}]^T \tag{17}$$

For any two SVs i and j, $\Delta c_{i,k}$ is assumed to be statistically uncorrelated from $\Delta c_{j,k}$. We distinguish two hypotheses, H_0 and H_1, which we define as:

$$\begin{aligned} \text{null hypothesis } H_0 : \Delta\gamma_k = 0 \implies J_k = J_{k-1} \text{ (no change jamming power)} \\ \text{alternate hypothesis } H_1 : \Delta\gamma_k > 0 \implies J_k > J_{k-1} \text{ (jamming power density increasing)} \end{aligned} \tag{18}$$

The PDF of the time-differenced C/N0 measurements under H_0 and H_1 can be written as:

$$\begin{aligned} p\left(\boldsymbol{\Delta c}_k | H_0\right) &= \frac{1}{\sqrt{(2\pi)^n |\boldsymbol{S}_{\Delta k}|}}\ exp\left(-\frac{1}{2}\boldsymbol{\Delta c}_k^T \boldsymbol{S}_{\Delta k}^{-1} \boldsymbol{\Delta c}_k\right) \\ p\left(\boldsymbol{\Delta c}_k | H_1\right) &= \frac{1}{\sqrt{(2\pi)^n |\boldsymbol{S}_{\Delta k}|}}\ exp\left(-\frac{1}{2}(\boldsymbol{\Delta c}_k + \mathbf{1}\Delta\gamma_k)^T \boldsymbol{S}_{\Delta k}^{-1} (\boldsymbol{\Delta c}_k + \mathbf{1}\Delta\gamma_k)\right) \end{aligned} \tag{19}$$

where $\boldsymbol{S}_{\Delta k} = diag\left(\left[\sigma^2_{\Delta 1,k} \dots \sigma^2_{\Delta n,k}\right]\right)$. The Neyman-Pearson optimal test using time-differenced C/N0s can be expressed as:

$$\Lambda_k(\boldsymbol{\Delta c}_k, \Delta\gamma_k) = ln\left(\frac{P\left(\boldsymbol{\Delta c}_k | \, H_1\right)}{P\left(\boldsymbol{\Delta c}_k | \, H_0\right)}\right) \tag{20}$$

Substituting Eq. 19 into Eq. 20 and simplifying, we get the following expression:

$$\Lambda_k(\boldsymbol{\Delta c}_k, \Delta\gamma_k) = -\boldsymbol{\Delta c}_k^T \boldsymbol{S}_{\Delta k}^{-1} \mathbf{1} \Delta\gamma_k - \frac{1}{2} \mathbf{1}^T \boldsymbol{S}_{\Delta k}^{-1} \mathbf{1} \Delta\gamma_k^2 \tag{21}$$

The locally most powerful test statistic as $\Delta\gamma_k \to 0$ can be expressed as:

$$\beta_k \triangleq \left. \frac{\partial \Lambda_k(\boldsymbol{\Delta c}_k, \Delta\gamma_k)}{\partial \Delta\gamma_k} \right|_{\Delta\gamma_k = 0} = -\boldsymbol{\Delta c}_k^T \boldsymbol{S}_{\Delta k}^{-1} \mathbf{1} \tag{22}$$

Under H_0, the detection test statistic β_k is distributed as follows:

$$\beta_k \sim N\left(0, \mathbf{1}^T \boldsymbol{S}_{\Delta k}^{-1} \mathbf{1}\right) \tag{23}$$

This test statistic is optimal for detecting small simultaneous drops in C/N0 across satellites.

The computation of β_k requires a model for the diagonal covariance matrix $\boldsymbol{S}_{\Delta k}$, which is evaluated as a function of satellite azimuth and elevation angle in Sec. III.

III. NOMINAL MODELS OF C/N0 MEASUREMENTS

In this section we develop a method for modeling the nominal mean and variance of C/N0 measurements, and the variance of time-differenced C/N0. The models are determined under H_0, i.e., using jamming-free C/N0 data.

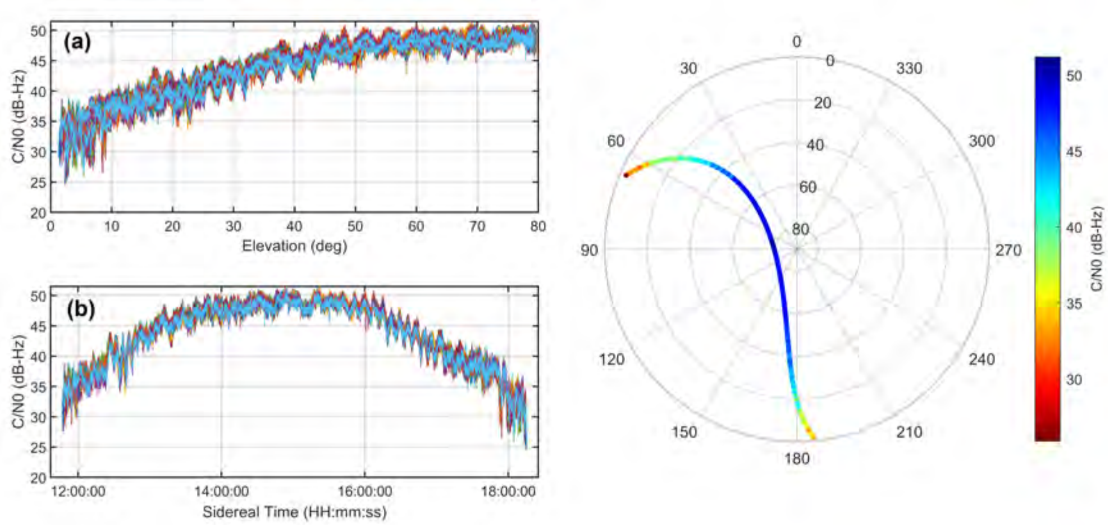

Figure 1: *LEFT:* GPS L1 C/N0 measurements for PRN8 at Charlotte, NC (CORS site index: NC77) during a week in May 2021, (a) as a function of elevation, and (b) as a function time over a sidereal day. The plots show 7 color-coded curves corresponding to 7 days. *RIGHT:* Color-coded C/N0 on an azimuth-elevation sky-plot for PRN8 on May 1, 2021. A single day is shown because azimuth-elevation curves overlap over multiple days.

In Fig.1, we used one month of GPS L1 C/N0 data from an NGS CORS station in Charlotte, North Carolina (NC) (CORS site index: NC77) [18]. Fig.1 shows that the mean and variance of C/N0 are repeatable from one sidereal day to another, and that C/N0 primarily varies with satellite elevation angle, and secondarily with satellite PRN and with azimuth angle.

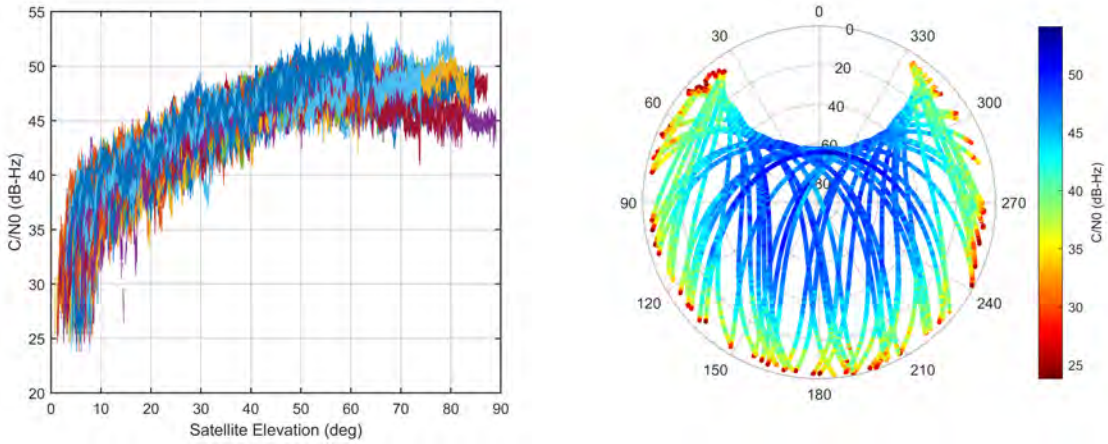

Figure 2: *LEFT:* GPS L1 C/N0 measurements for all SVs (color-coded) at Charlotte, NC over 24 hours as a function of elevation. *RIGHT:* Color-coded GPS L1 C/N0 measurements on an azimuth-elevation plot: elevation is clearly a major cause for C/N0 variations, but C/N0 values also vary with satellite and azimuth angle.

1. Elevation-Dependent C/N0 Mean and Overbounding Variance Model

Based on Figs.1 and 3, we model mean C/N0 variations versus elevation using a second-order polynomial, one per uninterrupted satellite pass, that can be expressed as:

$$\mu_{i,k} = a_{0,i} + a_{1,i}\theta_{i,k} + a_{2,i}\theta_{i,k}^2 \tag{24}$$

where, $\theta_{i,k}$ is the elevation of SV 'i' at time step 'k', and $[a_{0,i}\ a_{2,i}\ a_{1,i}]$ are the coefficients of the second order polynomial determined by curve fitting of experimental data.

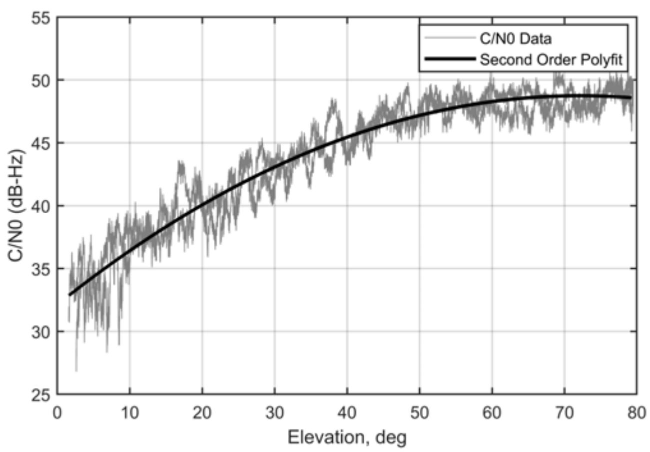

Figure 3: Mean C/N0 measurement model for PRN 8 at the example location of Charlotte, NC. We develop an automated method to derive such models for each satellite pass at each CORS station.

We determine the GPS L1 C/N0 variance model versus satellite elevation angle by first computing C/N0 residuals. These residuals are obtained by subtracting the mean model from sample C/N0 measurements, as shown in Fig.4. The elevation range is divided into 2.5 degree elevation bins. In each bin, the C/N0 residual sample standard deviation is computed. We use a two-term exponential function to fit the model to sample standard deviations versus elevation. The C/N0 standard deviations model at time step k for SV i is expressed as:

$$\hat{\sigma}_{i,k} = b_1 e^{-c_1\theta_{i,k}} + b_2 e^{-c_2\theta_{i,k}} \tag{25}$$

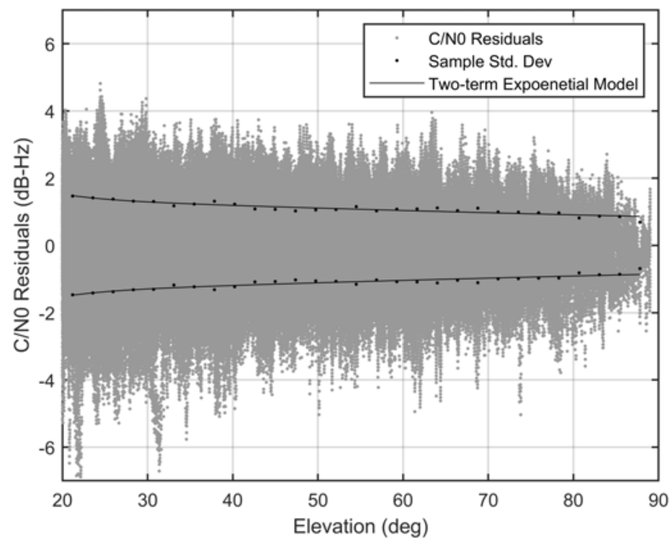

Figure 4: Sample and modeled standard deviations of C/N0 residuals (sample 'minus' mean) over 2.5-degree elevation bins. The grey data points are GPS L1 C/N0 residuals for all the SV over 24 hour at an example location (Charlotte, NC): variance decreases with SV elevation. The model (solid black line) is an elevation-dependent two-term exponential function.

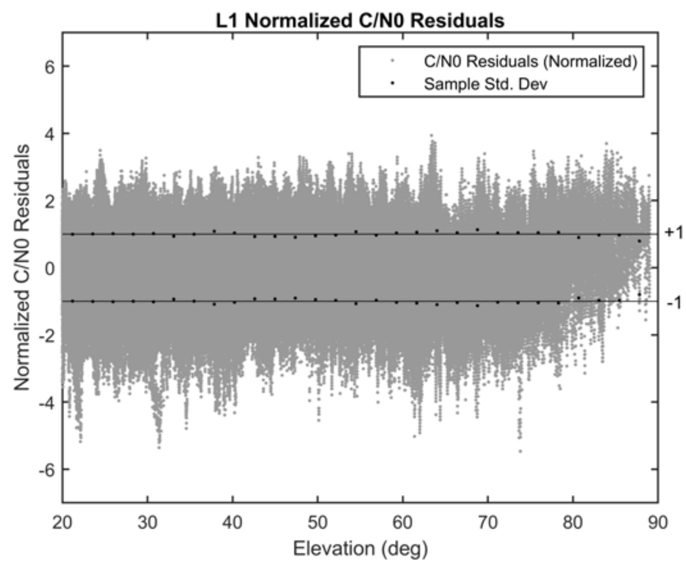

Figure 5: Normalized C/N0 measurement residuals (i.e., sample 'minus' mean model, divided by modeled standard deviation) as a function of elevation.

where we chose the coefficients b_1, b_2, c_1 and c_2 to be the same for all SVs. Fig.5 shows that C/N0 residuals normalized by their modeled standard deviation are zero mean with unit variance.

At this point, the elevation-dependent variance model accounts for 68% of the data, corresponding to one standard deviation (1-σ). However, the sample C/N0 distribution has wide tails, which must be accounted for when seeking a risk of false alert $P_{FA,REQ} < 32\%$. The quantile-to-quantile (QQ) representation in Fig.6 emphasizes the tails of the distribution. It shows the sample residual distribution (y-axis) versus the standard normal distribution (x-axis). For the model to be valid more than 68% of the time, the model's standard deviation must be inflated by a factor ζ_{OB}, which we determine using overbounding methods [19–21]. (The overbounding process had to account for all elevations and quantiles; we chose to model variations over elevations first, and then consider quantiles.) The overbounding, elevation-dependent standard deviation is expressed as:

$$\hat{\sigma}_{OB,i,k} = \zeta_{OB}\ \hat{\sigma}_{i,k}(\theta_{i,k}). \tag{26}$$

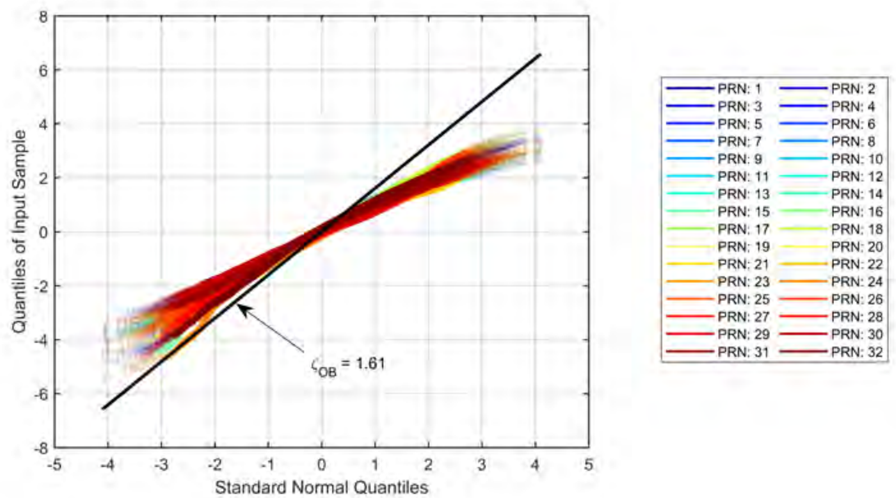

Figure 6: Gaussian overbounding of sample distribution of normalized C/N0 residuals.

2. Azimuth and Elevation Dependent C/N0 Measurement Variance Model

The left charts in Fig.1 show that C/N0 measurements are elevation-dependent, and that high-frequency variations repeat themselves from one satellite pass to the next over multiple sidereal days. These variations are not captured by the mean C/N0 model in Eq.24. If we account for such mean variations using a higher order model, then the C/N0 model variance can be tightened, which reduces detection thresholds and increases jamming detector sensitivity. On the other hand, for a fixed data set, the number of variance model parameters may increase, and fewer samples will be available to overbound the residual error (sample 'minus' mean) distribution. We will explore the trade-off between mean model accuracy and variance model fidelity to data. We derive a C/N0 measurement model as function of both satellite azimuth and elevation angles.

The top two charts in Fig.7 show again that the GPS L1 C/N0 measurement variations versus azimuth-elevation at the Charlotte, NC location are repeatable over the month month of May 2021. The mean C/N0 model shown with a black curve in the upper right-hand-side chart was obtained by partitioning data points for all jamming-free days in to azimuth-elevation bins along the trajectory. Eight days of data partitioned in 2880 bins are shown in the top right chart in Fig.7. In each bin, we computed the sample mean: the model (black curve) associates sample C/N0 mean values with azimuth-elevation bin centers.

The lower left-hand-side chart shows the residual C/N0 variations obtained by removing the mean model from the data. In each azimuth-elevation bin, similar to the mean model, we derive an azimuth-elevation-dependent variance model derived from the residual sample variance. The lower right-hand-side chart shows the residual normalized by the standard deviation model. An inflation factor is applied using the same overbounding method as in Eq.26.

As compared to the elevation-dependent model, each variance parameter here, one per bin, is derived using a much lower number of data points. This higher-dimensional model more accurately captures the mean C/N0 variations, but the variance model is of lower-fidelity because each parameter represents a smaller fraction of nominal conditions.

3. Elevation-Dependent Time-Differenced C/N0 Measurement Variance Model

The mean value of time-differenced C/N0 is negligibly small when the time interval between C/N0 measurements is one second or lower. We therefore assume that it is zero. Fig.8 illustrates this point by showing time-differenced C/N0 for all 32 GPS SVs over a day versus time, and versus satellite elevation. The time-differenced C/N0 nominal variance model is derived using the approach described in Sec.III.1.

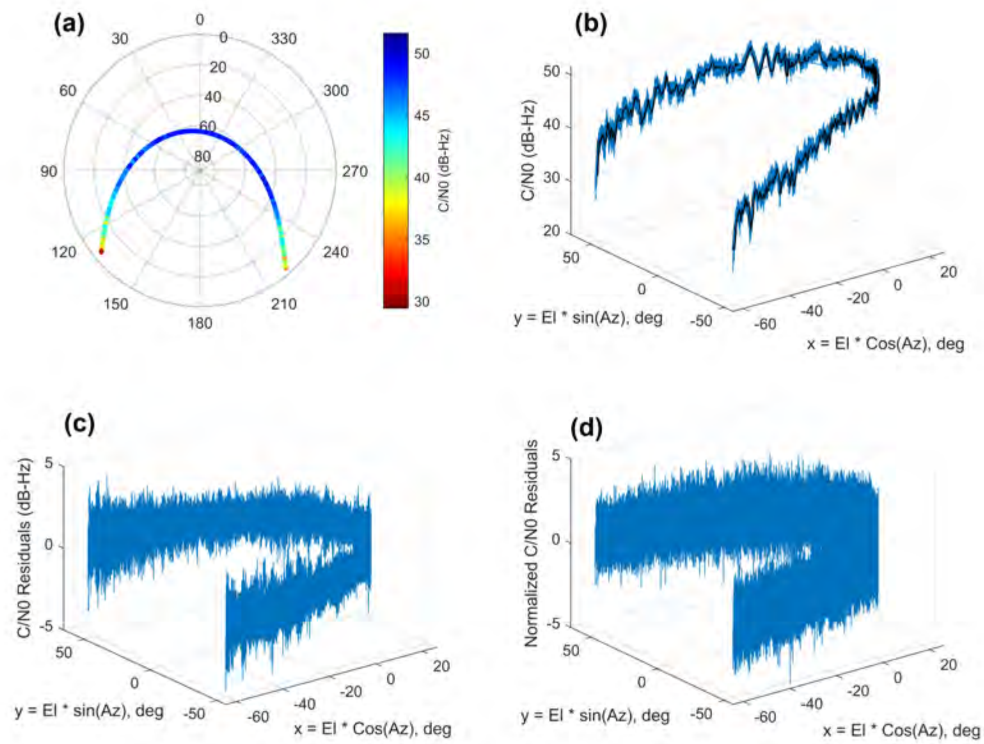

Figure 7: Overview of the azimuth-and-elevation-dependent C/N0 measurement modeling method. (a) Azimuth-elevation sky-plot for PRN2 at Charlotte, NC on May 1, 2021. (b) C/N0 measurements (blue) and C/N0 mean model (black). (c) C/N0 measurement residuals: samples 'minus' mean model. (d) Normalized C/N0 residuals: C/N0 residuals divided by modeled standard deviation.

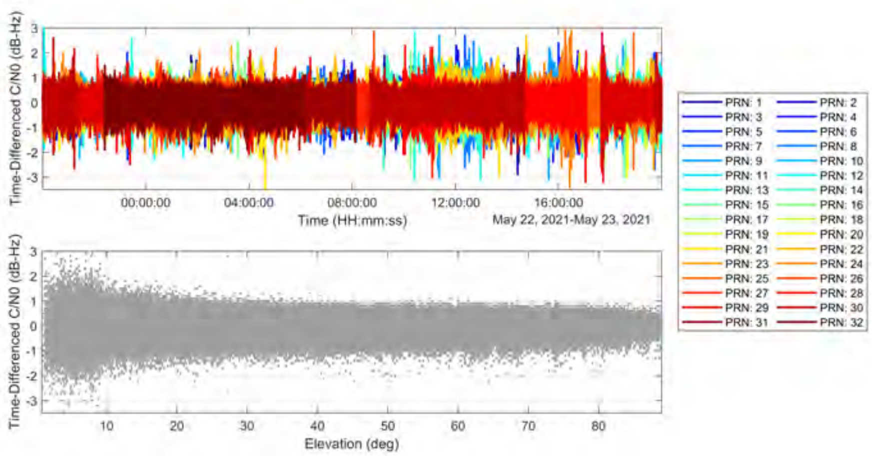

Figure 8: Time-differenced C/N0 measurements from all SVs over 24 hours (top). Time-differenced C/N0 measurements from all SVs over 24 hours as a function of elevation angle (bottom).

IV. EXPERIMENTAL EVALUATION OF C/N0-BASED JAMMING DETECTION METHODS

In this section, we evaluate the jamming detection methods using GPS L1 C/N0 data from CORS at an example location of Charlotte, NC (site index NC77; latitude: 35°7'21"N, longitude: 80°54'58"W). This site is located within 200 m from the intersection of Interstates I-77 and I-485, and next to a truck stop. It also provides data at 1 Hz sampling rate. It is therefore a good location for observing jamming events from PPDs.

The block diagram in Fig.9 gives an overview of the automated jamming detection method using CORS GPS observations data. The method includes deriving a nominal CORS-site-specific and satellite-specific C/N0 measurement model, incorporating this model in a jamming detector, and recording detected events. In order to derive the nominal model, jamming-event-free data must be selected. We have been using the time-differenced C/N0 detector to identify event-free data because it is effective with a coarse variance model and does not require a mean C/N0 model. Once event-free data is identified, nominal models are derived using one or more days of data and stored for each CORS site and satellite.

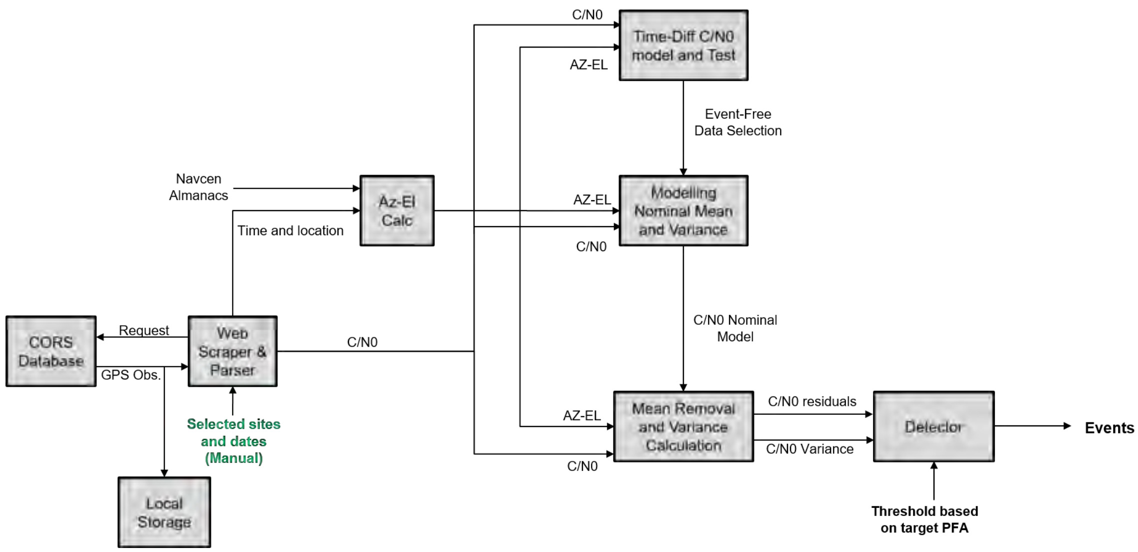

Figure 9: Block diagram illustrating the modeling process and jamming detection from CORS data.

1. What to Expect: Geometry of a Jammer Passing By a Static Roadside Receiver

In this subsection we present a theoretical model of an expected C/N0 drop caused by a PPD-type jammer passing by a static receiver, e.g., at a CORS site. The Friis equation for free-space propagation of signals is given by [22]:

$$P_r = P_t + G_r + G_t + 20\ log_{10}\left(\frac{\lambda}{4\pi d}\right) \tag{27}$$

where
P_r is the received power in dB,
P_t is the transmitted power in dB,
G_t is the receiving antenna gain in dB, in the direction of the transmitter,
G_t is the transmitting antenna gain in dB, in the direction of the receiver,
λ is the wavelength of the GPS L1 signal,
d is the distance between the transmitting and receiving antennas.

We make simplifying assumptions to get a rough idea of what jamming events to observe. Experimental results in [1] are insightful as well. We assume loss-less isotropic antennas with unit gains for both the receiver and transmitter. The GPS signal power is assumed to be -157 dBW and the thermal noise power density, N_0 is -201 dBW/Hz [23]. The jammer power is 9.5 mW for an RF-front end bandwidth of 20 MHz centered at GPS L1 frequency [24]. In actual data, we expect the observed C/N0 variations to vary with the type of PPD and receiver, the antenna gain patterns, and the antennas environment.

Still, can these assumptions inform us on how far away can a jammer be detected? For the scenario in Fig. 10, we simulate a truck-mounted jammer being driven at 70 mph by a CORS receiver located 250 m away from the road. The time-history of the distance between jammer and receiver is plotted on the bottom chart in Fig. 10 (c). The C/N0 curve over time is shown in the top chart. It shows that at the receiver may manage to keep track of the signal (C/N0 > 23 dB-Hz, and that detection must occur within a few seconds. We used data to verify that test statistics using time-windows are not more effective than instantaneous detectors.

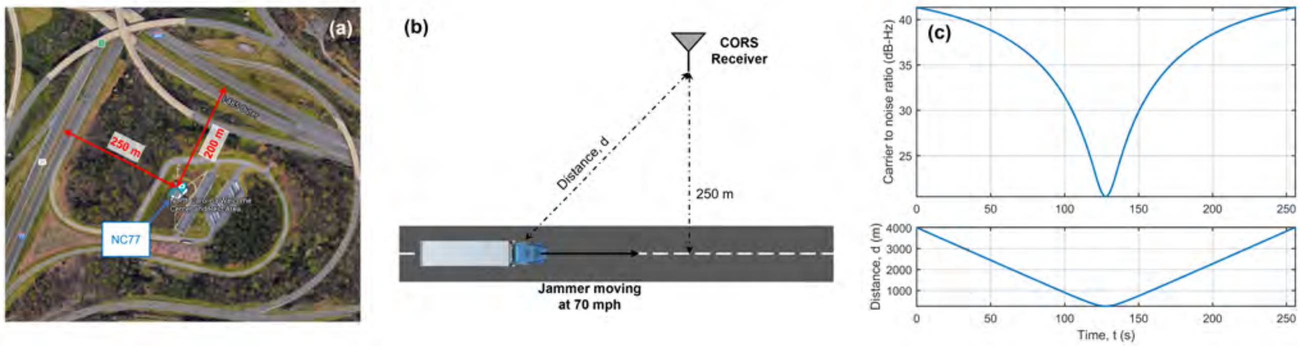

Figure 10: The geometry of Interstates around CORS site NC77 is shown on a map in (a). A schematic of a jammer passing by the CORS site is shown in (b). The resulting C/N0 time-history when a jammer is passing by the CORS site is shown in (c)

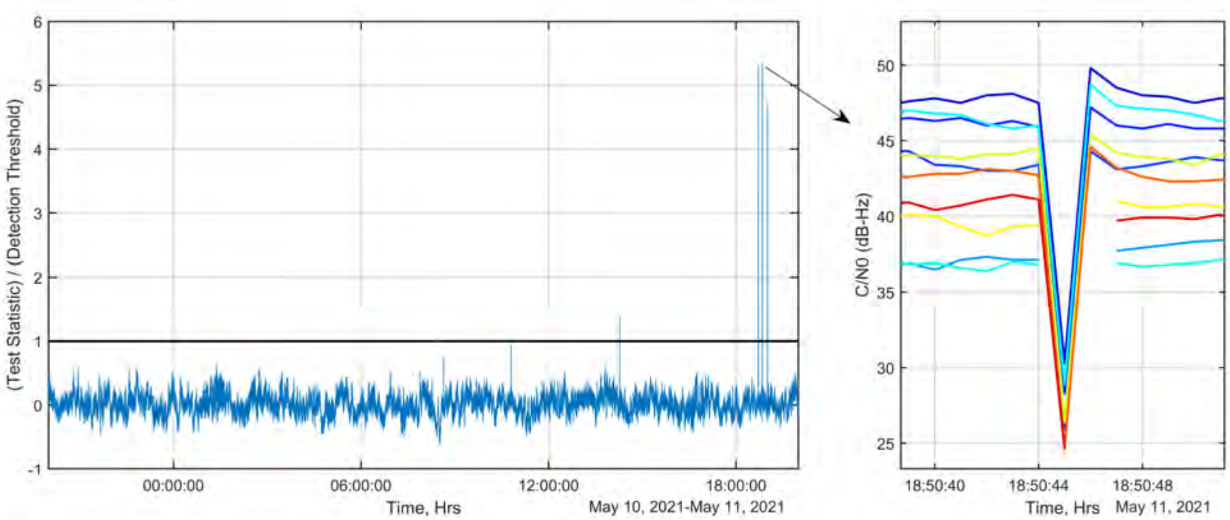

Figure 11: *LEFT:* Time history of the test statistic to threshold ratio on May 11, 2021. *RIGHT:* C/N0 from all SVs in view during an event.

2. Impact of C/N0 Modeling on Detection

This section evaluates the two detectors using the elevation-dependent model, and the azimuth-elevation dependent model described in Sec.III.1 and Sec.III.2. Both models can be used in the residual-projection test statistic in Eq.11 and its detection threshold in Eq.12. We implement a false alert requirement: $P_{FA,REQ} = 10^{-6}$. Fig.11 displays the ratio of the test statistic over the detection threshold on May 11, 2021. Jamming events are detected when this ratio exceeds 1. The right-hand-side chart in Fig.11 shows the GPS L1 C/N0 profile during one of the four detected events. The simultaneous decrease in C/N0 over all SVs is consistent with jamming by a PPD.

Fig.12 extends this analysis to multiple days. It complements the analysis of Fig.11 and it will reveal patterns in the detected events, for example, caused by PPD on trucks following a weekly schedule. The left-hand-side in Fig.11 shows the the test statistic to threshold ratio for the month of May: marker sizes are proportional to this ratio; weekends and weekdays are color-coded; red edges indicate ratios exceeding 1, i.e., detected events. The right-hand-side plot shows actual C/N0 profiles during one of the detected events.

Fig.13 shows the detection performance of the residual-projection test using the azimuth-elevation-dependent model. In this case, the detector is more sensitive and captures more events as compared to the elevation-dependent nominal model in 11. Also, test statistic variations causing "watermarks" in 11 are no longer present.

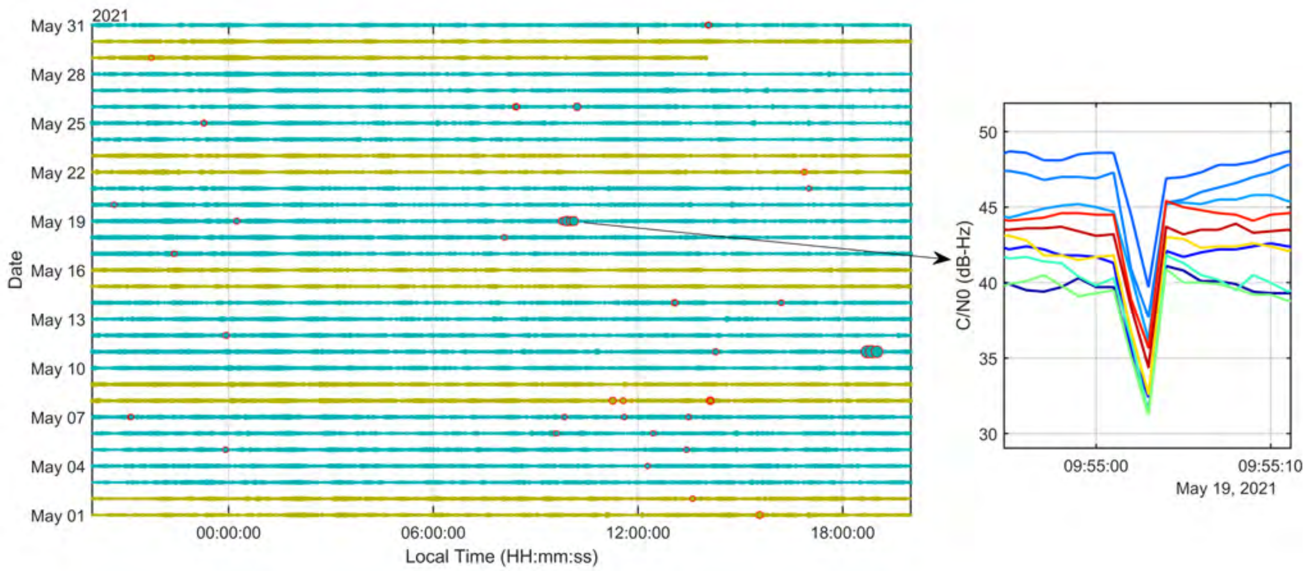

Figure 12: *LEFT:* One month of C/N0-based jamming monitoring using the elevation-dependent model at NC77 during May 2021. Two colors are used to distinguish weekends from weekdays. Marker size is proportional to the ratio of detection test-statistic to threshold. When this ratio exceeds the value of 1, the marker's edge is shown in red to indicate detection. Data is missing from the database on the 29^{th} of May. A watermark-like pattern appears caused by test statistic variations that repeat themselves daily with a 4-minute offset on this 24-hour range axis (variations repeat every sidereal day). *RIGHT:* C/N0 measurement profile for an example detected jamming event; satellites are color-coded.

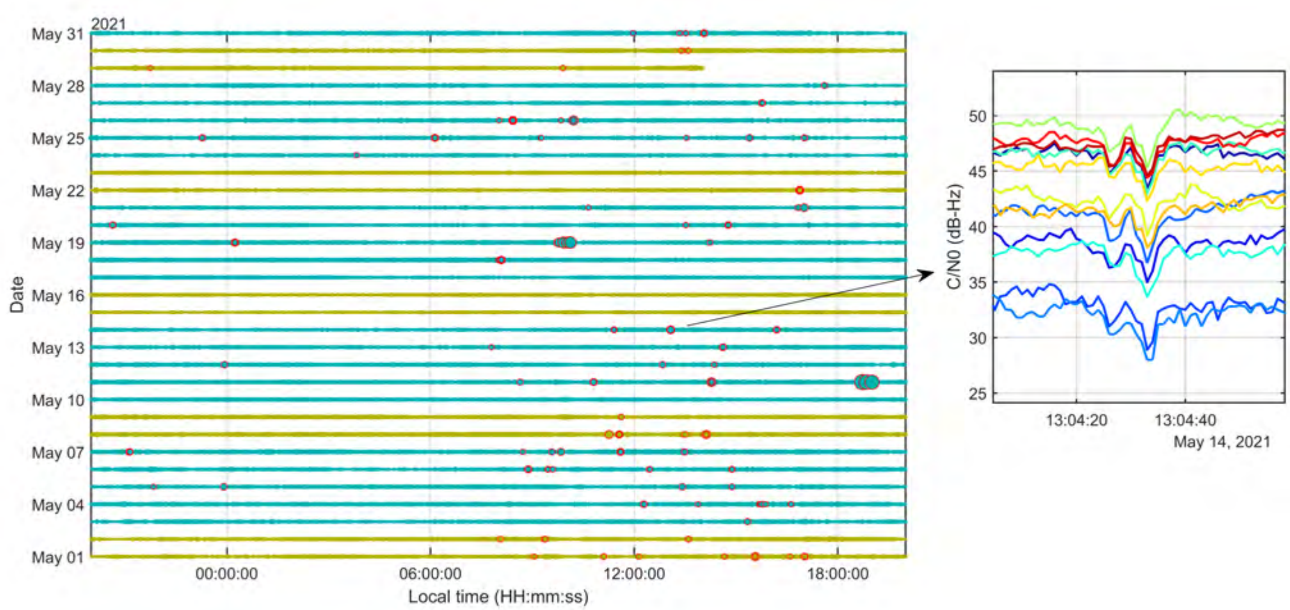

Figure 13: *LEFT:* Ratio of C/N0 test statistic over threshold using the azimuth-elevation-dependent model. Detected events shown with red marker edge. *RIGHT:* Example C/N0 measurement profile during one of the events.

3. Results of Time-Differenced C/N0 test

The time-differenced C/N0 test statistic in Eq.22 and its threshold in Eq.23 are evaluated in Fig.14 at NC77 over the month of May 2021. The time-differenced C/N0 detector's sensitivity is comparable to that of the C/N0 residual projection detector in Fig.13. We checked that all events on these two figures corresponds to simultaneous C/N0 drops on multiple satellites. Noteworthy in

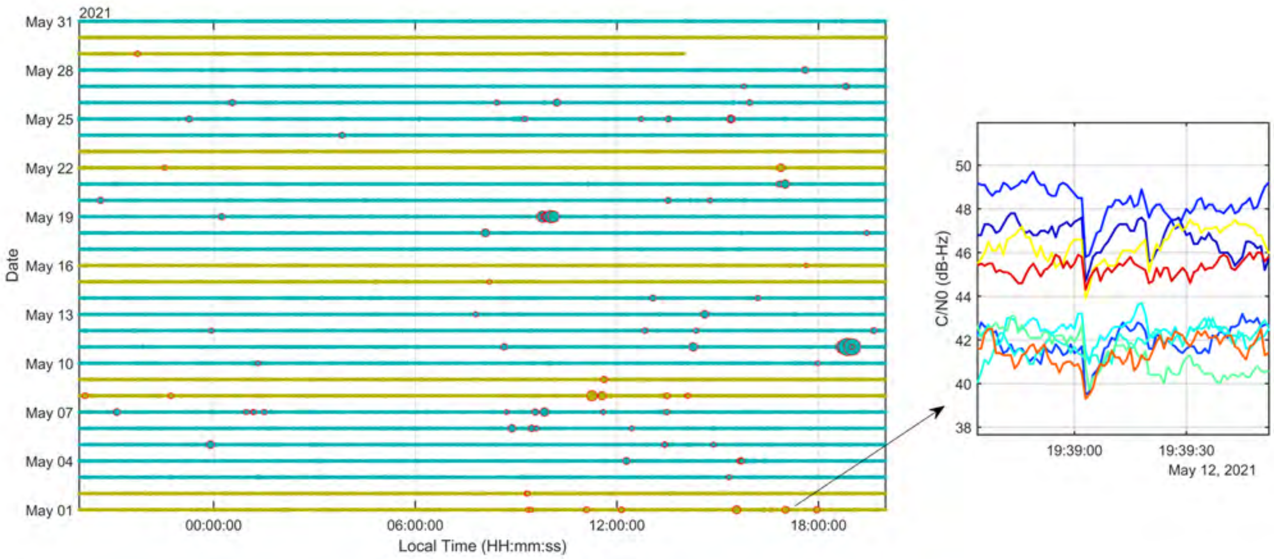

Figure 14: *LEFT:* Ratio of time-differenced C/N0 test statistic over threshold. Detected events shown with red marker edge. *RIGHT:* Example C/N0 time-profile during one of the events.

Fig.14 are the events occurring every Wednesday at midnight. We show the pattern of occurrence of events on Wednesdays over four months in Fig. 15.

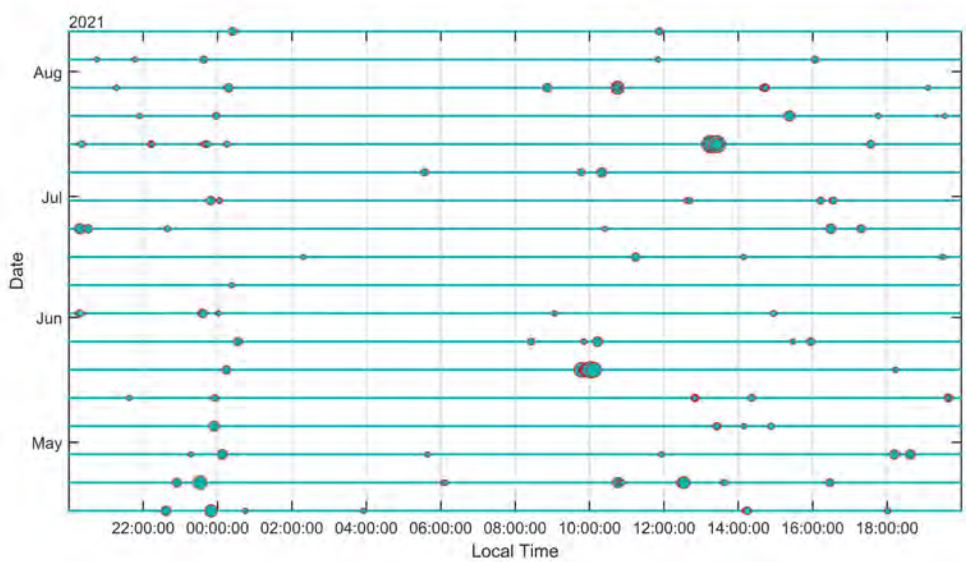

Figure 15: Detected events occurring on Wednesdays over four months at NC77. Repeated occurrences are found around midnight, local time.

V. CONSOLIDATING THE ANALYSIS OF DETECTED JAMMING EVENTS

In order to gain confidence on the fact that the detected events are actual jamming events, we use additional independent data from the following cases.

1. To identify jamming events caused by PPD devices onboard moving road vehicles, we analyze multiple CORS sites along a highway with the intention to observe sequences of events.

2. For strong jamming events affecting ground and air receivers over tens of kilometers, we evaluate whether events detected at CORS sites can also be observed using ADS-B data.

1. C/N0 Data Analysis for Multiple CORS Sites Along a Highway

We analyzed data from a pair of CORS sites along interstate I-40 in North Carolina over the month of May. The idea is to find pairs of events corresponding to road vehicles equipped with a jammer driving on I-40. The CORS site pair is NCCH and NCKN, which are separated by a 30-50 min drive time. The NCCH receiver and antenna is located 500 m from I-40 and NCKN is 5 km from I-40, but also 750 m from another state highway. Fig.16 shows jamming events detected over a month: red for detection at NCCH, blue for detection at NCKN. Pairs of detected events that could originate from a same jammer are boxed in black rectangles; the separation time between events are indicated. In future work, we will analyze other sites to find further evidence of jamming.

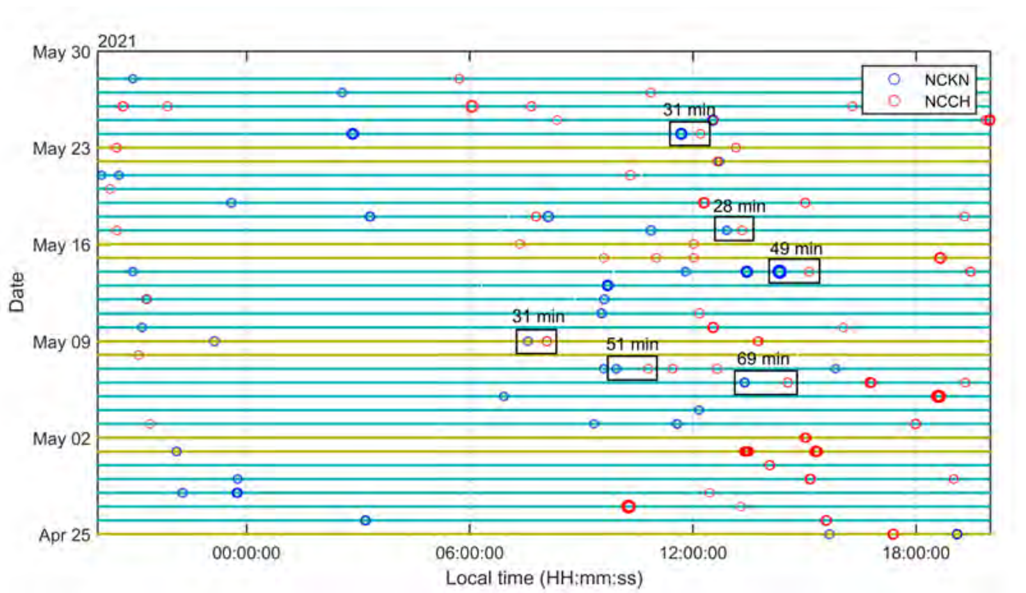

Figure 16: Detection events at two CORS sites along North Carolina Interstate 40 (NCKN and NCCH) over the month of May 2021. Detection pairs that could be caused by a same jammer are boxed, and the time-between-events is indicated.

2. ADS-B Data Analysis for Jamming Detection

ADS-B data was used from jamming detection in [9, 10]. These methods leverage aircraft receivers whose containment radius parameters broadcast in the ADS-B position messages can be used as RFI-indicators. Similarly, we analyze navigation integrity category (NIC) values over a region of interest to detect jamming.

Jamming of aircraft GNSS is likely caused by stronger signals than PPDs. We also count on the fact that the ground jammer is not only transmitting towards the sky, so that the jamming radius on the ground can reach several tens of kilometers. Therefore, we analyze CORS data in the region where we collect ADS-B data during two known jamming events. The two jamming events are the following.

1. The Marines Special Operations Command (MARSOC) performed GPS testing at Camp Lejeune, NC from the 1^{st} to the 21^{st} of March 2021. The details of the test are given in a Federal Aviation Administration (FAA)'s Notice to Airmen (NOTAM) [25]. The NOTAM stated that "testing may cause unreliable or unavailable GPS signal" over a radius of 45 nautical miles around Camp Lejeune.

2. A utility company's wireless control system signals was jamming GPS around the Wilmington, NC airport. Pilots reported interruptions to GPS at that time [26]. A notice to airmen (NOTAM) was issued on 18 November, 2020 about possible jamming over a 20 nautical mile radius around the Wilmington, NC airport.

We accessed the OpenSky-network ADS-B message database [27]. We collected ADS-B messages sent both during these events and under nominal jamming-free days, and within the regions mentioned in the NOTAMS. We parsed the messages to extract the aircraft positions and NIC values.

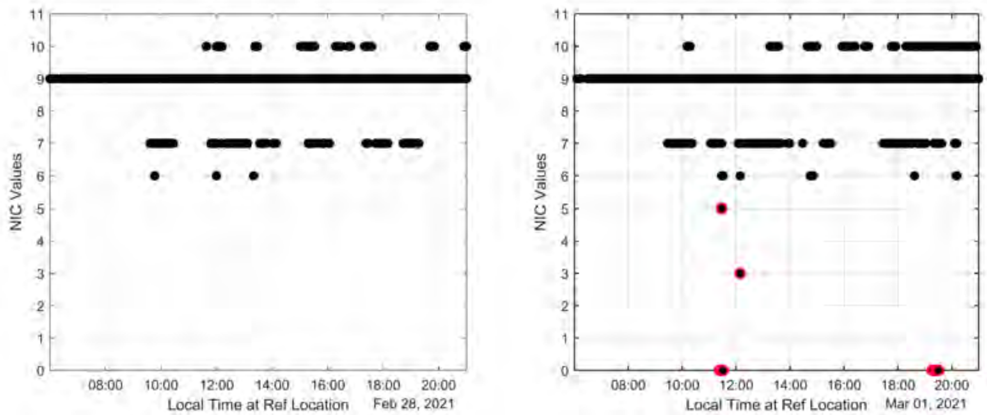

Figure 17: Comparison of NIC values over time during a nominal day (left) and during a military GPS testing day (right).

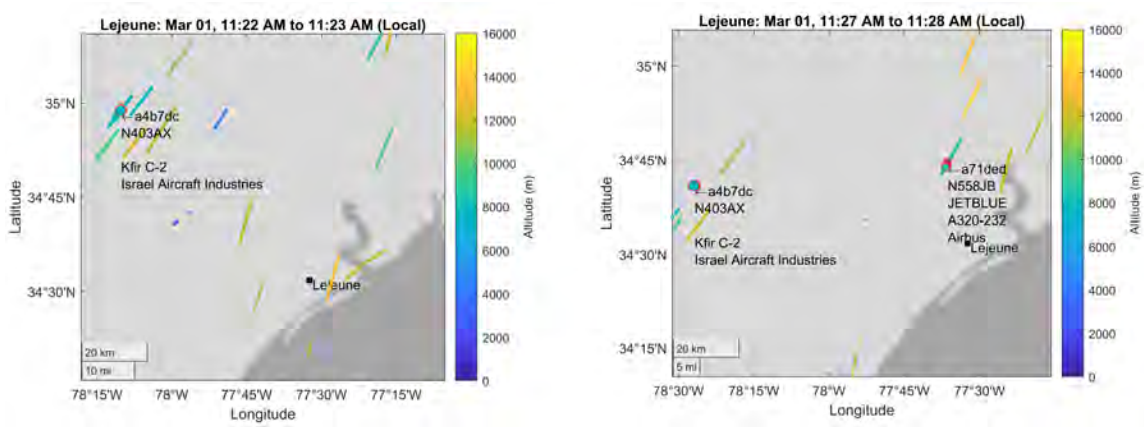

Figure 18: Color-coded NIC values for aircraft trajectories during MARSOC GPS testing at Camp Lejeune, NC. The marker size is proportional to the aircraft radius of containment. NIC values of 6 or lower are highlighted with red marker edges.

For the MARSOC GPS testing in March 2021, we found drops in NIC values on testing days which do not appear during nominal days. Fig.17 shows ADS-B NIC values over time on February 28, 2021 (when no testing occurred) and on March 1, 2021 (Day 1 of the test). We further analyzed the NIC drops at noon on March 1. We found that a military aircraft was reporting an NIC drop to zero and then a break in messages for 5 seconds. Within few minutes a commercial airliner reported a NIC drop from 9 to 6 due to a potential RFI.

Fig.18 shows one-minute intervals of reported aircraft positions in the test area. The marker size is inversely proportional to NIC values, i.e., proportional to the aircraft radius of containment. NIC values lower than or equal to 6 are indicated with a red marker edge. When an event is detected, the aircraft identifying information is displayed.

In parallel, we analyzed data from a CORS site (site index: NCJV) that is 20 km from the test center. Fig.19 shows an instance where ADS-B and CORS data both showed signs of a potential RFI. A commercial airliner flying over test site sent ADS-B messages with NIC values below 6 while CORS-site NCJV C/N0 data decreased for all satellites in view with an unusual wave-like pattern.

The second incident we investigated is one of unintended GPS jamming by a utility company near the Wilmington, NC airport [26]. On November 16 2020, commercial airliners flying near the Wilmington Airport reported NIC drops to 6. Fig.20 shows two time-intervals showing the NIC drops. We were not able to corroborate these events using CORS data.

VI. CONCLUSIONS AND FUTURE WORK

In this paper, we developed and evaluated new GNSS jamming detection methods for position navigation and timing (PNT) situational awareness. These methods must be automated because they are intended for data processing over large networks of

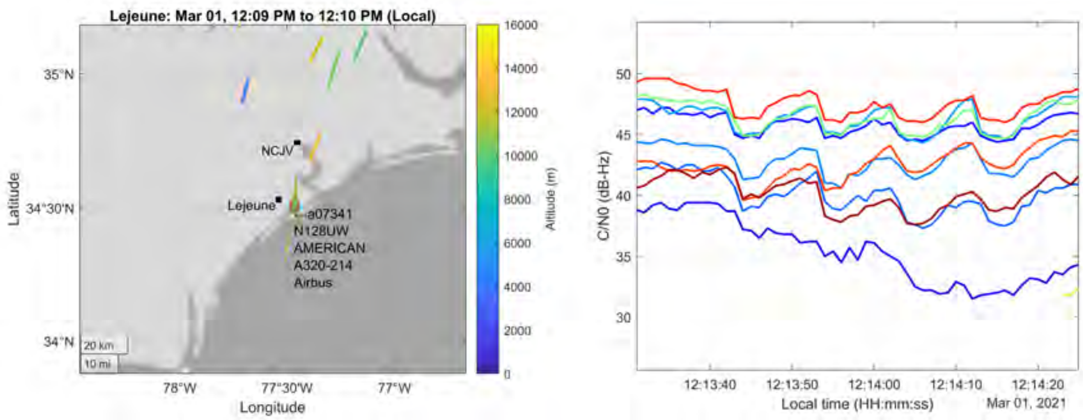

Figure 19: NCJV CORS site C/N0 data (right) during an NIC drop (left) during GPS testing by MARSOC at Camp Lejeune, NC

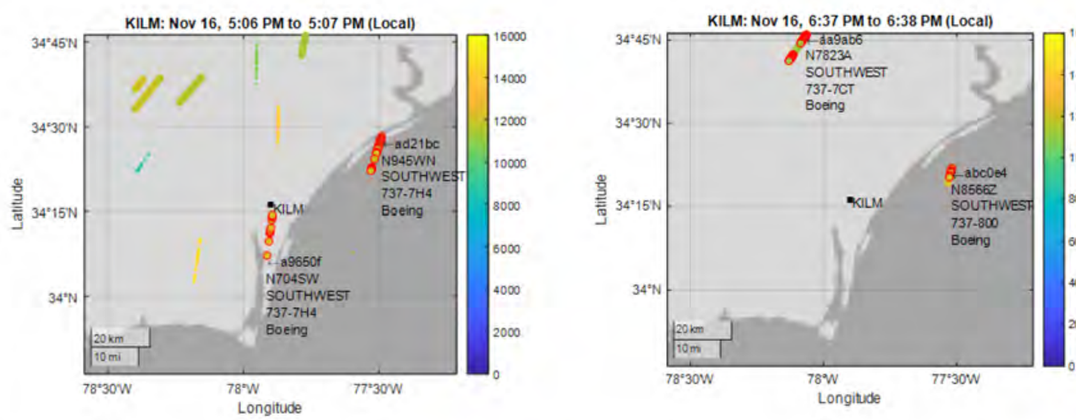

Figure 20: ADS-B reported NIC values showing possible jamming around the Wilmington Airport prior to issuance of a NOTAM by the FAA. Marker sizes are proportional to aircraft radii of containment. NIC values of 6 or lower are highlighted with red marker edges.

receivers. First, we derived C/N0-based jamming monitors aimed at detecting simultaneous drops in C/N0 across satellites. Then, we developed satellite and receiver-site-specific models of jamming-free C/N0 measurements. These models were incorporated in the jamming detection monitors to limit the risk of false alerts. This process was automated. Next, we analyzed GPS L1 data from continuously operating reference station (CORS). We evaluated the performance of the jamming monitors. We consolidated the fact that the detected events were caused by jamming by visual inspection, by data analysis over multiple days at multiple locations, and by further processing of ADS-B-reported aircraft receiver data during two known RFI events.

REFERENCES

[1] G. X. Gao, K. Gunning, T. Walter, and P. Enge, “Impact of personal privacy device for WAAS aviation users,” in *Proceedings of the 25th International Technical Meeting of The Satellite Division of the Institute of Navigation (ION GNSS 2012)*, 2012, pp. 235–241.

[2] “Above us only stars,” C4ADS (non-profit organization), Tech. Rep., 2019, Accessed on: December 13, 2020. [Online]. Available: https://www.c4reports.org/aboveusonlystars

[3] T. E. Humphreys, B. M. Ledvina, M. L. Psiaki, B. W. O’Hanlon, and P. M. Kintner, “Assessing the spoofing threat: Development of a portable GPS civilian spoofer,” in *Proceedings of the 21st International Technical Meeting of the Satellite Division of The Institute of Navigation (ION GNSS 2008)*, 2008, pp. 2314–2325.

[4] R. H. Mitch, “Model-based estimation techniques applied to Global Navigation Satellite System jammers,” Ph.D. dissertation, Cornell University, 2014.

[5] M. R. Mosavi, M. J. Rezaei, M. Pashaian, and M. S. Moghaddasi, “A fast and accurate anti-jamming system based on wavelet packet transform for GPS receivers,” *GPS solutions*, vol. 21, no. 2, pp. 415–426, 2017.

[6] K. D. Wesson, J. N. Gross, T. E. Humphreys, and B. L. Evans, “GNSS signal authentication via power and distortion monitoring,” *IEEE Transactions on Aerospace and Electronic Systems*, vol. 54, no. 2, pp. 739–754, 2017.

[7] C. Hegarty, B. O’Hanlon, A. Odeh, K. Shallberg, and J. Flake, “Spoofing detection in GNSS receivers through cross-ambiguity function monitoring,” in *Proceedings of the 32nd International Technical Meeting of the Satellite Division of the Institute of Navigation (ION GNSS+ 2019)*, 2019, pp. 920–942.

[8] N. S. Levigne, “Automatic gain control measurements as a GPS L1 interference detection metric,” Master’s thesis, University of Colorado at Boulder, 2019.

[9] E. B. Ala’Darabseh and B. Tedongmo, “Detecting GPS jamming incidents in Opensky data,” in *Proceedings of the 7th OpenSky Workshop*, vol. 67, 2019, pp. 97–108.

[10] Z. Liu, S. Lo, and T. Walter, “Characterization of ADS-B performance under GNSS interference,” in *Proceedings of the 33rd International Technical Meeting of the Satellite Division of The Institute of Navigation (ION GNSS+ 2020)*, 2020, pp. 3581–3591.

[11] M. R. Manesh and N. Kaabouch, “Cyber-attacks on unmanned aerial system networks: Detection, countermeasure, and future research directions,” *Computers & Security*, vol. 85, pp. 386–401, 2019.

[12] L. Scott, “J911: The case for fast jammer detection and location using crowdsourcing approaches,” in *Proceedings of the 24th International Technical Meeting of The Satellite Division of the Institute of Navigation (ION GNSS 2011)*, 2011, pp. 1931–1940.

[13] H.-P. Kim, G.-G. Jin, and J.-H. Won, “GNSS cloud-data processing technique for jamming detection, identification, and localisation,” *IET Radar, Sonar & Navigation*, vol. 14, no. 8, pp. 1143–1149, 2020.

[14] D. Miralles, N. Levigne, D. M. Akos, J. Blanch, and S. Lo, “Android raw GNSS measurements as the new anti-spoofing and anti-jamming solution,” in *Proceedings of the 31st International Technical Meeting of the Satellite Division of The Institute of Navigation (ION GNSS+ 2018)*, 2018, pp. 334–344.

[15] L. Strizic, D. M. Akos, and S. Lo, “Crowdsourcing GNSS jammer detection and localization,” in *Proceedings of the 2018 International Technical Meeting of The Institute of Navigation*, 2018, pp. 626–641.

[16] K. L. Strandjord and P. Axelrad, “A framework for regional GNSS situational awareness,” in *Proceedings of the 30th International Technical Meeting of The Satellite Division of the Institute of Navigation (ION GNSS+ 2017)*, 2017, pp. 2452–2466.

[17] D. Borio and C. Gioia, “Real-time jamming detection using the sum-of-squares paradigm,” in *2015 International Conference on Localization and GNSS (ICL-GNSS)*. IEEE, 2015, pp. 1–6.

[18] “National Geodetic Survey’s CORS Network.” [Online]. Available: https://geodesy.noaa.gov/CORS/

[19] B. DeCleene, “Defining pseudorange integrity-overbounding,” in *Proceedings of the 13th International Technical Meeting of the Satellite Division of The Institute of Navigation (ION GPS 2000)*, 2000, pp. 1916–1924.

[20] J. Rife, S. Pullen, P. Enge, and B. Pervan, “Paired overbounding for nonideal LAAS and WAAS error distributions,” *IEEE Transactions on Aerospace and Electronic Systems*, vol. 42, no. 4, pp. 1386–1395, 2006.

[21] J. Blanch, T. Walter, and P. Enge, “A MATLAB toolset to determine strict Gaussian bounding distributions of a sample distribution,” in *Proceedings of the 30th International Technical Meeting of The Satellite Division of the Institute of Navigation (ION GNSS+ 2017)*, 2017, pp. 4236–4247.

[22] L. d. A. Faria, C. A. Silvestre, M. A. F. Correia, and N. A. Roso, “GPS jamming signals propagation in free-space, urban and suburban environments,” *Journal of Aerospace Technology and Management*, vol. 10, 2018.

[23] E. D. Kaplan and C. Hegarty, *Understanding GPS/GNSS: principles and applications*. Artech house, 2017.

[24] R. H. Mitch, R. C. Dougherty, M. L. Psiaki, S. P. Powell, B. W. O’Hanlon, J. A. Bhatti, and T. E. Humphreys, “Signal characteristics of civil GPS jammers,” in *Proceedings of the 24th International Technical Meeting of the Satellite Division of The Institute of Navigation (ION GNSS 2011)*, 2011, pp. 1907–1919.

[25] Federal Aviation Authority, “NOTC1698 - FLIGHT ADVISORY - GPS Interference Testing,” Circular, February 2021, Accessed on: March 01, 2021. [Online]. Available: https://www.faasafety.gov/spans/noticeView.aspx?nid=11698

[26] Virginia Department of Transportation, “Utility company jams GPS near airport,” News Brief, January 2021, Accessed on: February 01, 2021. [Online]. Available: https://doav.virginia.gov/calendar-and-news/news/2021-january/utility-company-jams-gps-near-airportnew-page/

[27] “Open-Sky Network (non-profit association),” Accessed on: March, 2020. [Online]. Available: https://opensky-network.org/